University of Nebraska - Lincoln

DigitalCommons@University of Nebraska - Lincoln

2012

Tuning of the size and the lattice parameter of ion-beam synthesized Pb nanoparticles embedded in Si

Huan Wang
Instituut voor Kern-en Stralingsfysica and INPAC, K.U. Leuven, Belgium, huan.wang@fys.kuleuven.be

J. Cuppens
Laboratorium voor Vaste-Stoffysica en Magnetisme and INPAC, K.U. Leuven, Belgium

E. Biermans
Elektronenmicroscopie voor Materiaalonderzoek, Universiteit Antwerpen

S. Bals
Elektronenmicroscopie voor Materiaalonderzoek, Universiteit Antwerpen

Lucia Fernandez-Ballester
University of Nebraska - Lincoln, lucia.fernandez@unl.edu

See next page for additional authors

Follow this and additional works at: https://digitalcommons.unl.edu/engineeringmechanicsfacpub

Part of the Mechanical Engineering Commons

Authors

Huan Wang, J. Cuppens, E. Biermans, S. Bals, Lucia Fernandez-Ballester, K. O. Kvashnina, W. Bras, M. J. Van Bael, K. Temst, and A. Vantomme

Tuning of the size and the lattice parameter of ion-beam synthesized Pb nanoparticles embedded in Si

Huan Wang[1], J Cuppens[2], E Biermans[3], S Bals[3], L Fernandez-Ballester[4,5], K O Kvashnina[4], W Bras[4], M J Van Bael[2], K Temst[1] and A Vantomme[1]

[1] Instituut voor Kern-en Stralingsfysica and INPAC, K.U. Leuven, Celestijnenlaan 200D, 3001 Leuven, Belgium

[2] Laboratorium voor Vaste-Stoffysica en Magnetisme and INPAC, K.U. Leuven, Celestijnenlaan 200D, 3001 Leuven, Belgium

[3] Elektronenmicroscopie voor Materiaalonderzoek, Universiteit Antwerpen, Groenenborgerlaan 171, 2020 Antwerp, Belgium

[4] DUBBLE @ ESRF, 6 Rue Jules Horowitz, 38043 Grenoble, France

E-mail: huan.wang@fys.kuleuven.be

Abstract

The size and lattice constant evolution of Pb nanoparticles (NPs) synthesized by high fluence implantation in crystalline Si have been studied with a variety of experimental techniques. Results obtained from small-angle x-ray scattering showed that the Pb NPs grow with increasing implantation fluence and annealing duration. The theory of NP growth kinetics can be applied to qualitatively explain the size evolution of the Pb NPs during the implantation and annealing processes. Moreover, the lattice constant of the Pb NPs was evaluated by conventional x-ray diffraction. The lattice dilatation was observed to decrease with increasing size of the Pb NPs. Such lattice constant tuning can be attributed to the pseudomorphism caused by the lattice mismatch between the Pb NPs and the Si matrix.

(Some figures may appear in colour only in the online journal)

1. Introduction

Nanoparticles (NPs) and nanostructured materials (NSs) have attracted increasing attention in the materials community [1, 2] since their structural, electronic, magnetic, optical, catalytic, mechanical and thermodynamic properties are significantly different from those of either the bulk or a single molecule [1, 3]. The lattice parameter for a given structure can be influenced by the grain size—this is a well-known phenomenon in both NSs, such as a metallic film with nanometre-sized crystallites, and isolated NPs, such as NPs on amorphous substrates [4]. In the case of nanostructured single phase materials, a lattice expansion is commonly observed, and explained by a stress field caused by excess volume in the grain boundaries [4–9]. Elemental NPs are found to exhibit a lattice contraction, which is explained by surface tension effects [4, 10–12]. Both effects exist also for larger particles, but only at the nanoscale is the surface-to-volume ratio large enough to influence the entire particle. The properties of a crystalline phase are closely connected to its lattice parameters. Changes in lattice parameter can, depending on the material under consideration, be expected to influence, e.g. mechanical, magnetic, thermal and electrical properties. For instance, systems on the border of an electronic Mott-transition, such as vanadium oxide, exhibit a drastically different electrical conductivity when the lattice parameter is changed [13]. Similarly, several materials have a large tendency to change their magnetic configuration dramatically when the lattice parameter is changed. For example, the fcc phase of Fe, which can be stabilized at low temperatures as precipitates in

[5] Current address: Department of Engineering Mechanics and Mechanical Engineering, University of Nebraska at Lincoln, Lincoln, NE 68588, USA.

a Cu matrix, is one of the several which are known to display this behaviour [14]. For semiconducting systems, the observed coupling between the magnitude of the band gap and the lattice constant is of particular interest [15].

The situation for embedded metallic NPs having an epitaxial interface with a crystalline matrix is less well studied compared with isolated NPs or single phase nanostructured materials. In this case, an interesting opportunity for lattice constant tuning via the lattice mismatch between the NPs and the crystalline matrix can be exploited. Such a pseudomorphic distortion influence on the lattice constant is generally observed in epitaxial thin films [16], i.e. the elastic deformation of the pseudomorphic layers completely compensates the lattice mismatch between thin films and their substrates. Moreover, for sufficiently small particles, the lattice parameter variation may be directly correlated with a change in the material's properties.

Among different possible techniques, ion-beam synthesis has been proven to be a suitable method in obtaining embedded NPs. The research activity in this field is stimulated by the possibility to produce high volume fractions of NPs with specific properties and potential applications in, e.g., nanoelectronics and nanophotonics [17–19]. In a previous study [20], it was found that Pb NPs grow in a cube-on-cube alignment with respect to the crystalline Si matrix after high fluence implantation and subsequent annealing, leading to the formation of an epitaxial particle/matrix interface. Such a system is very suitable for investigating the pseudomorphic modification of the lattice constant of the Pb NPs: (i) the lattice mismatch between bulk Pb and Si is as large as −9.7%; and (ii) the solubility of Pb in Si is extremely low, even at the melting point of Pb [21], implying that the lattice constant will not be influenced by mixing with the matrix element.

In this paper, we first describe the procedure to control the size of Pb NPs by employing different implantation fluences and annealing time intervals. The average radius of the Pb NPs can be accurately determined with a combination of synchrotron-based small-angle x-ray scattering (SAXS) and transmission electron microscopy (TEM). The influence of implantation fluence and annealing duration on the final size of the Pb NPs is investigated and discussed within the theory of NP growth kinetics during the implantation and thermal annealing processes. In addition, the effect of pseudomorphic growth on the lattice constant and the elastic strain of the embedded Pb NPs was studied as a function of their size by x-ray diffraction (XRD).

2. Experimental

Single-crystal Si (1 0 0) wafers have been implanted with 80 keV Pb$^+$ ions. The current density during the implantation process was maintained constant at $2 \, \mu\text{A cm}^{-2}$ in order to reduce sample heating and to keep a constant relation between the implantation time and fluence. Due to the limited projected range, R_p, of the implanted ions ($R_p \sim 38$ nm) calculated with SRIM [22], after implantation, a 70 nm Si capping layer was deposited to avoid surface oxidation during the annealing process. The Pb fluence was accurately determined by Rutherford backscattering spectrometry. Two sets of samples, all annealed at 600 °C in N$_2$ atmosphere, were prepared: (i) with the same annealing duration (45 min) but implantation fluences ranging from 0.5×10^{16} to $2.0 \times 10^{16} \, \text{cm}^{-2}$; and (ii) with a fixed implantation fluence ($1.0 \times 10^{16} \, \text{cm}^{-2}$) but an annealing duration varying from 5 min to 4 h. Depending on the applied characterization techniques, we either implanted one side (for XRD and TEM) or both sides (for SAXS) of the Si wafers. For the latter experiments, double side polished Si (1 0 0) wafers with a thickness of only 60 μm were used to maximize the scattered x-ray signal.

Size determination of the Pb NPs was performed by SAXS experiments, carried out at the Dutch-Belgian beamline 'DUBBLE' (BM26B) at the European synchrotron radiation facility (ESRF) in Grenoble [23]. The sample was oriented perpendicularly to the incident x-ray beam ($\lambda = 0.142$ nm, $E = 10$ keV, beam size 0.2 mm × 0.2 mm). The scattered x-rays were detected by a two-dimensional multiwire gas-filled detector at a distance of 4 m behind the sample. The scattering vector q ($q = 4\pi \sin\theta/\lambda$, where θ is the scattering angle) was calibrated using a silver behenate diffraction pattern [24]. The scattered signals were acquired for typically 60 min and radially integrated, so that a one-dimensional data set in the scattering vector range $q = 0.2$–$1.0 \, \text{nm}^{-1}$ was obtained.

Electronic tomography, which was used for an independent size determination, was performed on a JEOL 3000 transmission electron microscope operated at 300 kV. First, a micro-pillar sample prepared by focused ion beam was mounted on a dedicated on-axis tomography holder [25]. Then a series of high angle annular dark field-scanning transmission electron microscopy (HAADF-STEM) images are acquired over a tilt range ±90° with 2° tilt angle increments. Finally, these images serve as an input for three-dimensional (3D) image reconstruction based on the mathematical algorithm simultaneous iterative reconstruction technique (SIRT) [26]. The size evaluation by both techniques is complementary in the sense that SAXS provides information averaged in the x-ray illuminated (exploratory) area on the targets whereas electron tomography yields 3D information on a (limited) number of individual NPs in a relatively small area as the diameter of a micro-pillar sample is typically less than 2 μm.

As a well-developed technique, XRD is widely used to determine the lattice constant and the strain of epitaxial layers [27] or nanocrystals [28]. Its accuracy has been proven complementarily by, e.g., x-ray absorption fine structure [29], TEM [30], channelling [31], etc, especially for lattice variations within 1%. In our work, conventional XRD was performed on a Bruker D8 diffractometer system at room temperature, using Cu K$_\alpha$ radiation with an x-ray wavelength of 0.1542 nm. We used 2θ–θ scans to identify the crystalline Pb precipitates and their lattice constants. XRD azimuthal Φ scans combined with conventional (two-dimensional) high resolution TEM measurements performed on a JEOL 4000 operated at 400 keV were applied for determining the fcc-structure and crystallographic orientation of the Pb NPs embedded in Si.
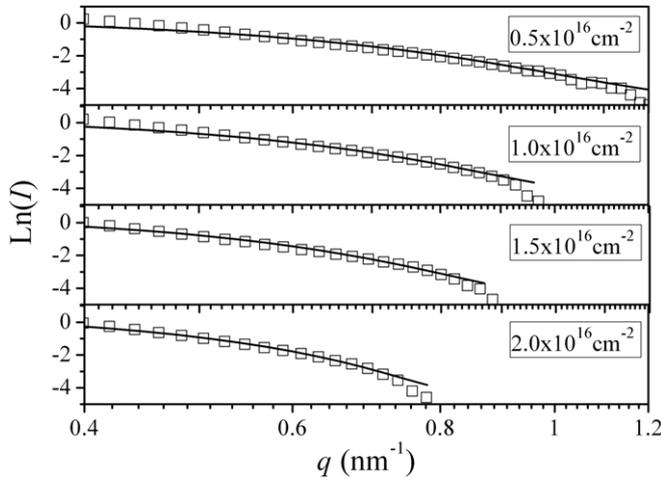
Figure 1. Small-angle scattering patterns from samples with different implantation fluences. The solid lines represent the spherical model fits to the experimental data.

3. Results and discussions

3.1. Size determination and evolution of Pb NPs

As an adequate method for size determination of NPs embedded in a thin matrix, non-destructive SAXS measurements are widely used. In the case of a diluted assembly of spherical particles, neglecting particle interaction, the scattering intensity is given by [32]

$$I(q) \propto \int f(R) V(R)^2 P(q, R)\, dR \qquad (1)$$

where $V(R)$ and $P(q, R)$ are the volume and form factor, respectively, of a sphere of radius R. The form factor of the sphere is given by [32]

$$P(q, R) = \left[\frac{3\{\sin(qR) - qR\cos(qR)\}}{(qR)^3} \right]^2. \qquad (2)$$

To obtain the particle size distribution, we assumed that the number density of the sphere of radius R follows a Gaussian distribution, $f(R)$, where

$$f(R) = \frac{1}{\sigma\sqrt{2\pi}} e^{-[(R-R_0)^2/2\sigma^2]}. \qquad (3)$$

Least square refinement yields two parameters, R and σ, where the latter is the standard deviation.

Figure 1 shows the measured SAXS profiles for the samples with different implantation fluences. For each data set, the signal from a corresponding virgin Si substrate of equivalent thickness was subtracted. Moreover, the signal was corrected for the detector response function. The scattering curves of the samples with higher implantation fluence have a stronger fall-off because for larger NPs the x-rays are preferably scattered into a smaller q-range. Thus, for large q-values the signal is noisier and closer to the background. Quantitative analysis is performed in a q-range 0.4–1.2 nm^{-1}, which is associated with a feature particle radius of $R = \pi/q = 7$–2 nm, i.e. the typical radius of the Pb NPs. The changes

Table 1. Average radius (R_{SAXS}) and radius distribution (σ_R) of the Pb NPs determined by SAXS, after implantation using different fluences and annealing times (annealing was done at 600 °C).

Sample No	Fluence (cm^{-2})	Annealing time (min)	R_{SAXS} (nm)	σ_R (nm)
1	0.5×10^{16}	45	2.7 ± 0.5	2.6 ± 0.5
2	0.8×10^{16}	45	3.2 ± 0.3	2.6 ± 0.3
3	1.0×10^{16}	45	3.5 ± 0.3	3.1 ± 0.3
4	1.5×10^{16}	45	4.3 ± 0.3	3.1 ± 0.3
5	2.0×10^{16}	45	5.0 ± 0.3	2.8 ± 0.3
6	1.0×10^{16}	5	3.0 ± 0.3	2.8 ± 0.3
7	1.0×10^{16}	90	3.7 ± 0.2	3.1 ± 0.3
8	1.0×10^{16}	160	4.3 ± 0.2	3.1 ± 0.3
9	1.0×10^{16}	240	4.8 ± 0.3	3.1 ± 0.3

observed in SAXS patterns clearly indicate that the NPs grow as a function of implantation fluence. The corresponding sphere model fits of the experimental SAXS data are indicated by the solid curves in figure 1. R_{SAXS} and $\sigma_R = 2.35\sigma$ (i.e. the half-width of the radius distribution) are deduced from the obtained fitting parameters (see table 1). The error on the SAXS data is mainly caused by the thickness variation of the Si substrates ($\pm 2\,\mu$m) resulting in a change of the scattering curves after subtracting the virgin Si signal.

A 2D TEM image of sample 3 (with implantation fluence of 1.0×10^{16} and annealed at 600 °C for 45 min) clearly shows Pb NPs embedded in a crystalline Si substrate below a 70 nm amorphous Si cap layer (figure 2(*a*)). A visualization of the 3D reconstruction of the sample is shown in figures 2(*b*) and (*c*) revealing separated, spherically shaped Pb NPs. This observation gives strong support for the validity of assuming spherically shaped NPs in the SAXS data analysis. The size distribution for sample 3 extracted from the 3D reconstruction of the volume is plotted in figure 2(*d*); an average radius of Pb NPs $R_{TEM} = 3.3 \pm 0.2$ nm is obtained, in good agreement with the SAXS results ($R_{SAXS} = 3.5 \pm 0.3$ nm). Moreover, the presence of a discontinuous 2D Pb thin layer at the interface between the crystalline Si substrate and the amorphous cap layer is observed, which may be attributed to a high mobility of Pb at grain boundaries of the interface [33].

In order to describe the size evolution of the Pb NPs under our experimental conditions, the classical nucleation and growth theory which has been developed for ion implanted systems can be applied [34, 35]. The formation and growth of Pb NPs during ion implantation can be divided into three distinct stages:

(i) Supersaturation: immediately after the start of the ion implantation, the impurity atoms are introduced into the host matrix. The supersaturation $S(t) = [C(t) - C_\infty]/C_\infty$ increases linearly as a function of the implanted ion fluence f, in which $C(t)$ is the concentration of monomers at a given time t, and C_∞ is the bulk solubility. During the initial stage of the implantation, $S(t)$ increases further and reaches a critical value S_C at a time t_1, after which small agglomerates of impurity atoms (e.g. dimers, trimers, etc) start to form, i.e. spontaneous nucleation sets in. Since ion implantation is a non-equilibrium process, it is worth emphasizing that the concentrations of the implanted
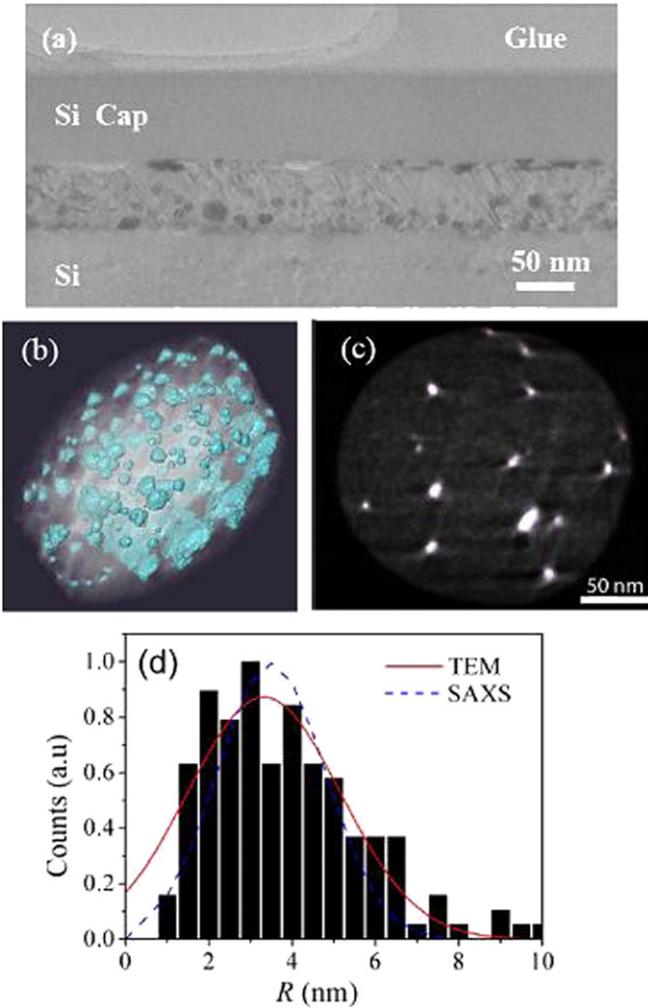
Figure 2. (*a*) Cross-sectional TEM image, (*b*) A vortex rendering of the 3D reconstruction of the volume showing the spherically shaped Pb NPs and a 2D Pb layer, (*c*) A slice through the 3D reconstructed volume and (*d*) size distribution histogram obtained from the TEM data of sample 3, the solid lines compare the size distributions obtained from TEM and SAXS.

dopants in a solid matrix can be much higher than the bulk solubility, i.e. $S \gg 0$.

(ii) Nucleation: as $S(t)$ exceeds S_C, the tiny agglomerates constitute a pool of embryos, and some of them grow (by statistical fluctuations) beyond a critical radius R_C can occur, thus forming stable precipitates. Here, R_C is the critical radius above which a particle spontaneously grows and below which it dissolves. These stable embryos act as sinks for diffusing impurity atoms. Despite the continuing implantation of impurities, the supersaturation $S(t)$ starts to decrease, thus eventually dropping below the threshold for nucleation at a time t_2. The time span $t_1 < t < t_2$ is usually referred to as the nucleation regime.

(iii) Growth: the nucleation of new particles is inhibited below S_C, and all the existing NPs grow by absorbing newly implanted impurity atoms rather than by competitive ripening. The system in such a free-growth regime is characterized by a constant supersaturation S_0. The diffusion of monomers to the particle surface drives the

NPs' growth. The growth rate of the spherically shaped particles in the diffusion limit can be written as [36–38]

$$\frac{dR}{dt} = \frac{DV_a(C_0 - C_\infty)}{R}\left(1 - \frac{R_C}{R}\right) \qquad (4)$$

where R is the particle radius, D is the diffusion coefficient, V_a is the molar volume. For $R_C/R \ll 1$ during the implantation process, integration of equation (4) reveals that the diffusion limited growth is characterized by a $R \propto t^{1/2}$ behaviour.

Since in our case the ion-beam current was kept constant during the implantation process, $t \propto f$ can be assumed. Therefore, the average radius of the Pb NPs at the end of the implantation (R_A) is expected to follow $R_A \propto f^{1/2}$.

During the subsequent annealing, the Pb NPs continue to evolve in a *closed system*, in which the total mass of Pb is conserved. At the beginning of the annealing, a transient period appears during which $S(t)$ reaches a quasi-steady state [35, 36]. The particles can grow directly by solute depletion of the surrounding matrix without competing with the growth of any other particles [36], i.e. a purely diffusion limited growth regime. The growth rate given by equation (4) is then still valid. Hence, the analytical expression for $R(t_a)$, the average radius of spherical precipitates as a function of annealing duration t_a, is

$$R^2(t_a) = R_A^2 + 2DV_a(C_S - C_\infty)t_a \qquad (5)$$

in which $(C_S - C_\infty)$ defines the degree of supersaturation during the initial annealing stage. Since the supersaturation cannot stay constant indefinitely due to mass conservation, it must eventually decrease again. At this stage, the system switches from the growth regime to the Ostwald ripening (OR) regime: the particles whose radius is smaller than the actual value of the critical radius become unstable and dissolve, while larger ones continue to grow by consuming the dissolved material. The description of the size evolution of spherical particles in an OR regime during this final stage was first developed by Lifshitz and Slyozov [39], and Wagner [40] and is now known as the LSW theory:

$$R^3(t) - R_0^3 = \frac{8}{9}\frac{\sigma V_a^2 C_e}{\kappa_B T}Dt \qquad (6)$$

where R_0 is the average particle radius at the beginning of the OR regime, σ is the surface tension of the particles, C_e is the equilibrium solute concentration in the matrix and κ_B is the Boltzmann constant.

For the samples implanted with the same fluence and current at room temperature (samples 3, 6–9), the average radius of the Pb NPs after implantation, R_A, is basically the same. During the annealing process, the particles are expected to grow with increasing annealing duration as can be clearly seen in table 1. However, it should be mentioned that, based on the available data and error bars, it is impossible to distinguish which NP growth model best describes the annealing process, since both the R^2 and R^3 increase linearly with the annealing time t_a within the experimental error (figure 3).

As mentioned above, for the samples with a varying implantation fluence f, the average radius of the Pb NPs after
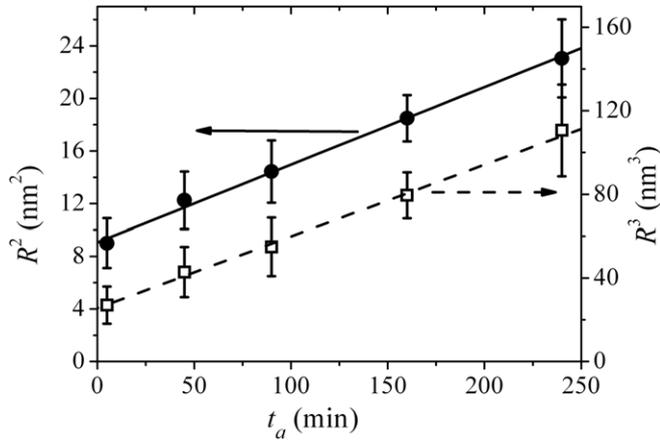
Figure 3. R^2 (●) and R^3 (○) versus annealing time t_a at 600 °C (samples 3, 6–9), the solid and dashed lines are linear fits to the experimental data.
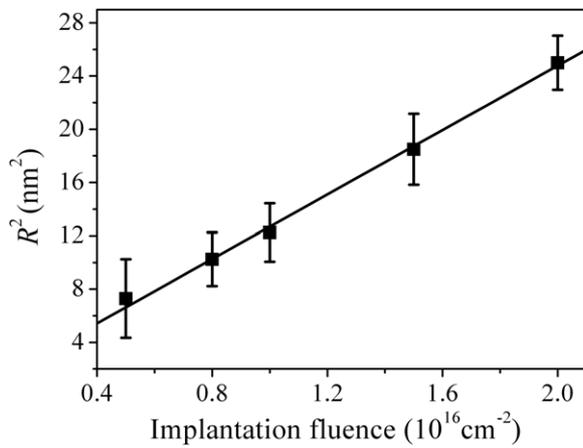

Figure 5. XRD 2θ–θ scans of Pb implanted Si for various implantation fluences. The data sets are shifted vertically for clarity.

Figure 4. R^2 versus implantation fluence f (samples 1–5), the solid line is the linear fit to the experimental data.

Figure 6. XRD Φ scans for fcc-Pb (1 1 1) and Si (1 1 1) ($\chi \sim 54.8°$).

implantation can be expected to scale with fluence as $f^{1/2}$. After annealing under the same conditions (600 °C, 45 min), $R \propto f^{1/2}$ is theoretically predicted. Indeed, from figure 4, it can be seen that R^2 increases linearly with f, consistent with the growth model, although it is impossible to extract the diffusion coefficient D due to the unknown supersaturation S_0, i.e. C_0, during the implantation process.

3.2. Crystallographic orientation and lattice constants of the fcc-Pb NPs

XRD is used to identify the Pb crystalline precipitates in Si after annealing. Figure 5 shows the XRD 2θ–θ scans for samples 3, 4 and 5 (table 1) implanted with varying fluence and a virgin Si wafer, in a 2θ range 30°–80°. The two small sharp peaks located at 61.6° and 65.9° are due to the contributions of the residual Cu K$_\beta$ and Ni K$_\alpha$ radiation for the Si (4 0 0) diffraction peak, respectively.

For all the implanted samples, the only Pb peak that can be detected is the Pb (2 0 0) diffraction peak at $2\theta \approx 36.3°$, confirming that the Pb particles are highly oriented with respect to the host matrix [20]. The diffraction peaks sharpen with
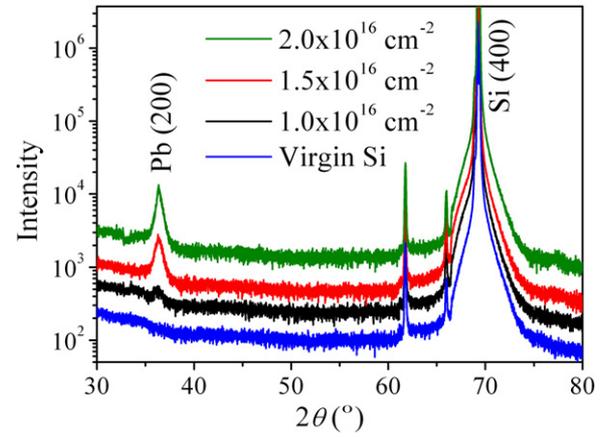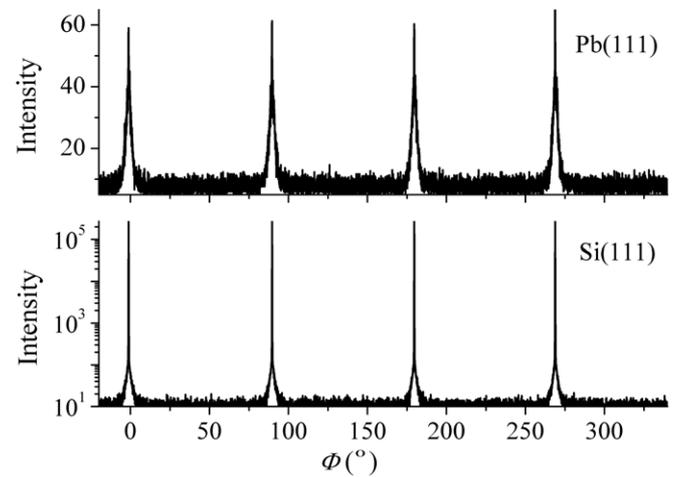
increasing fluence, indicating the increasing size of the Pb NPs, as deduced above.

Azimuthal Φ scans of the diffraction planes not parallel with the sample surface (i.e. tilted by an angle χ from the sample surface) help us to determine the Pb NPs lattice structure and also to reveal their crystallographic in-plane orientation with respect to the Si matrix. Figure 6 shows the Φ scans for the Pb (1 1 1) diffraction with $2\theta \approx 31.3°$ and Si (1 1 1) diffraction with $2\theta \approx 28.5°$, respectively. The fourfold symmetry, with $\chi \approx 54.8°$, is consistent with the fcc-Pb (1 1 1) Φ scan viewed along the [2 0 0] direction. The peak positions of Pb (1 1 1) are the same as the ones of Si (1 1 1), indicating a cube-on-cube epitaxial relationship between the Pb NPs and the Si matrix. Therefore, we can conclude that the fcc-Pb NPs are crystallographically oriented with respect to the Si matrix according to Pb (2 0 0) [0 0 2]‖Si (2 0 0) [0 0 2]. Figure 7(*a*) shows a high resolution TEM image of a Pb NP. The image clearly indicates the faceted epitaxial Pb/Si interface and the orientation alignment between the Pb NP and the crystalline Si matrix.

Formation of Pb NPs growing in parallel alignment with the Si matrix after implantation and subsequent annealing is in good agreement with earlier observations [20, 41, 42], where
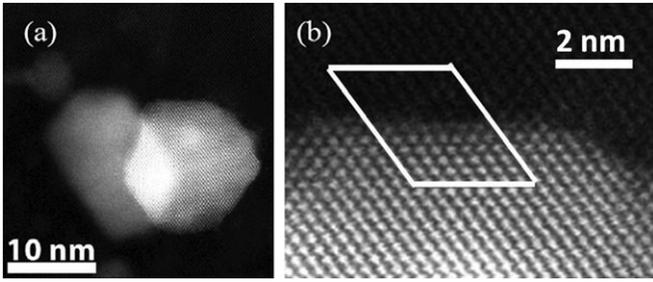
J. Phys. D: Appl. Phys. **45** (2012) 035301

H Wang *et al*

Figure 7. (*a*) High resolution TEM image corresponding to the [0 1 1] zone axis, showing the epitaxial Pb/Si interface; (*b*) zoom in of the Pb/Si interface, the Burgers circuit indicates the presence of a misfit dislocation.
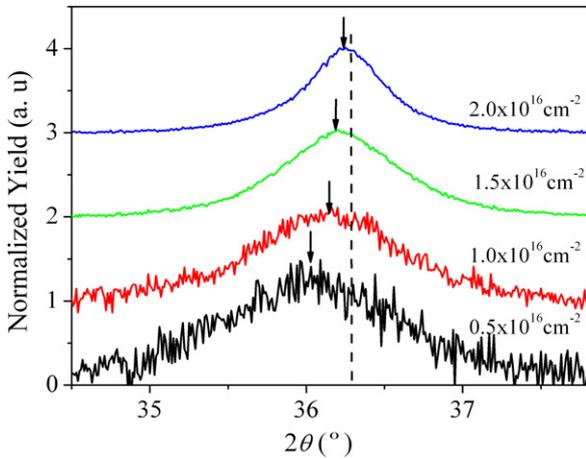

Figure 8. XRD 2θ–θ scans for samples with different implantation fluences after annealing, revealing a size-dependent out-of-plane tensile strain in the Pb NPs. The dashed line indicates the position of the bulk Pb (2 0 0) diffraction peak; the arrows show the peak positions for the NPs.

TEM was used to verify the existence of aligned Pb NPs. In addition, the hexagonal shape of the Pb NP perpendicular to the Si [0 1 1] zone axis (figure 7(*a*)) indicates that the particle shape is a truncated octahedron bounded by {1 1 1} and {0 0 1} planes. Our results are also consistent with previous investigation of Pb NPs in Si [20, 41].

In order to accurately determine the lattice constants of the Pb NPs, XRD signals from the Pb NPs were carefully monitored by symmetric 2θ–θ measurements with 2θ ranging between 34.5° and 38.2°. The Pb (2 0 0) diffraction profiles of the samples with different implantation fluences are plotted in figure 8 after subtracting the background signal. It can be seen that all peak positions deviate from the bulk Pb value and that the deviation increases with decreasing average particle size. Taking the Si (4 0 0) peak as a reference, the lattice constant c_{epi} of the Pb NPs has been calculated. Subsequently, the perpendicular strain of the Pb NPs $e^{\perp} = (c_{epi} - c_b)/c_b$ is deduced, using $c_b = 0.495$ nm for bulk (fully relaxed) Pb [43] (see table 2). The positive value of $e^{\perp}$ indicates that the Pb NPs are under tensile strain.

The in-plane lattice constant, a_{epi}, is determined from 2θ–θ scans of the (2 2 0) diffraction combined with the results from (2 0 0) scans. According to the *d* spacing equation for a cubic crystal,

$$d^2_{(h\,k\,l)} = \frac{1}{\frac{k^2}{c^2} + \frac{l^2}{a^2} + \frac{h^2}{a^2}} \quad (7)$$

substituting the measured values of $d_{(2\,2\,0)}$, $c = c_{epi}$ (table 2), and the values $k = 2$, $l = 2$, $h = 0$ into the equation, we obtain the values for a_{epi} and the estimated error. From these values, the parallel strain of the Pb NPs $e^{\parallel} = (a_{epi} - a_b)/a_b$ can be deduced (table 2). The in-plane lattice parameter for the sample with the lowest implantation fluence could not be calculated due to the low diffraction intensity. From table 2, we find that the lattice constant of the Pb NPs increases with decreasing NP size and is consistently larger than the bulk value. In addition, the uniform elastic tensile strain of the embedded Pb NPs, i.e. $e^{\perp} \approx e^{\parallel}$, can be also identified.

For an epitaxial thin layer, as its thickness becomes larger than a critical value (typically 1–2 nm for a metallic layer), misfit dislocations are introduced at the interface to reduce the strain energy of the epitaxial layer. Similarly, in our case the positive values of $e^{\perp}$ and $e^{\parallel}$ for Pb NPs in Si are quite small and cannot be explained by simple pseudomorphic growth, which predicts a significantly larger strain value of 9.7% if the Pb NPs would accommodate exactly the same lattice constant as the surrounding Si matrix, i.e. a one-to-one connection between Pb planes and Si planes. It can be speculated that during the annealing at high temperature (i.e. 600 °C) the Si matrix was re-crystallized and liquid Pb NPs (the melting point of bulk Pb is 327 °C) were present in Si. During the cooling process, the Pb NPs solidify and align with the Si matrix by an epitaxial interface. Due to the large lattice mismatch between the Si matrix and the Pb NPs, misfit dislocations at the interface are introduced (see figure 7(*b*)), releasing the strain energy. Since the Pb NPs are embedded in Si, their lattice can be enlarged isotropically via the epitaxial interface resulting in $e^{\perp} \approx e^{\parallel}$. The observed decrease in the lattice expansion with increasing size of the Pb NPs can be attributed to (i) the reduction of surface-to-volume ratio and (ii) increasing dislocation density at the particle/matrix interface. Both are expected to reduce the fraction of pseudomorphic Pb at the interface with increasing particle size. According to our results, it can be extrapolated that Pb NPs embedded in Si with a radius of about 6.5 nm will be fully relaxed with the same annealing conditions. To the best of our knowledge, such lattice constant tuning of metallic NPs embedded in a crystalline matrix due to the lattice mismatch with the epitaxial interface has not been previously reported.

4. Conclusions

In this work, the dependence of the size of Pb NPs embedded in a Si matrix on the implantation fluence and annealing duration was investigated complementarily by SAXS and TEM. The size evolution of Pb NPs with varying implantation fluence and annealing duration can be explained by the theory of the growth kinetics for NPs during implantation and subsequent thermal annealing processes. Moreover, quantitative XRD studies demonstrate that the isotropic lattice expansion ($e^{\perp} \approx e^{\parallel}$) increases with decreasing particle radius. Such a result can be qualitatively explained by two competing effects, i.e. the

J. Phys. D: Appl. Phys. **45** (2012) 035301

H Wang *et al*

Table 2. Lattice constants and elastic strain of the Pb NPs extracted from the XRD measurements.

Sample No	Implantation fluence $(1 \times 10^{16}\ cm^{-2})$	Average radius (nm)	c_{epi} (nm)	a_{epi} (nm)	$e^{\perp}$ (%)	$e^{\parallel}$ (%)
1	0.5	2.7	0.4983 ± 0.0006	—	0.67 ± 0.12	—
3	1.0	3.5	0.4971 ± 0.0006	0.4968 ± 0.0006	0.42 ± 0.13	0.36 ± 0.13
4	1.5	4.3	0.4963 ± 0.0006	0.4961 ± 0.0006	0.26 ± 0.14	0.22 ± 0.14
5	2.0	5.0	0.4958 ± 0.0006	0.4961 ± 0.0006	0.16 ± 0.16	0.22 ± 0.14

influence of pseudomorphic growth on the lattice expansion of the Pb NPs due to lattice mismatch and the reduction of the lattice expansion via the formation of misfit dislocations in order to decrease the strain energy.

It can be expected that a wide variety of materials' properties which drastically depend on the elastic strain such as thermal and superconducting properties can be tuned by experimentally tailoring the lattice parameters.

Acknowledgments

References

[1] Sun C Q 2009 *Prog. Mater. Sci.* **54** 179
[2] Gleiter H 2000 *Acta Mater.* **48** 1
[3] Di W H, Willinger M G, Ferreira R A S, Ren X G, Lu S Z and Pinna N 2008 *J. Phys. Chem.* C **112** 18815
[4] Zhu Y F, Zheng W T and Jiang Q 2009 *Appl. Phys. Lett.* **95** 083110
[5] Liu X D, Zhang H Y, Lu K and Hu Z Q 1994 *J. Phys.: Condens. Matter* **6** L497
[6] Lu K and Zhao Y H 1999 *Nanostruct. Mater.* **12** 559
[7] Banerjee B, Sperling E A, Thompson G B, Fraser H L, Bose S and Ayyub P 2003 *Appl. Phys. Lett.* **82** 4250
[8] Qin W, Nagase T, Umakeoshi Y and Szpunar J A 2008 *Phil. Mag. Lett.* **88** 169
[9] Qin W, Nagase T, Umakeoshi Y and Szpunar J A 2007 *J. Phys.: Condens. Matter* **19** 236217
[10] Qi W H and Wang M P 2005 *J. Nanopart. Res.* **7** 51
[11] Huang Z, Thomson P and Di S 2007 *J. Phys. Chem. Solids* **68** 530
[12] Jiang Q, Liang L H and Zhao D S 2001 *J. Phys. Chem.* B **105** 6275
[13] Poteryaev A I, Tomczak J M, Biermann S, Georges A, Lichtenstein A I, Rubstov A N, Saha-Dasgupta T and Andersen O K 2007 *Phys. Rev.* B **76** 085127
[14] Tsunoda Y 1989 *J. Phys.: Condens. Matter* **1** 10427
[15] Harrison W A 1980 *Electronic Structure and the Properties of Solid the Physics of the Chemical Bond* (New York: Dover)
[16] Renaud G, Barbier A and Robach O 1999 *Phys. Rev.* B **60** 5872
[17] Gonella F and Mazzoldi P 2000 *Handbook of Nanostructured Materials and Nanotechnology* (San Diego, CA: Academic)
[18] Meldrum A, Boatner L A and White C W 2001 *Nucl. Instrum. Methods Phys. Res.* B **178** 7
[19] Mazzoldi P and Mattei G 2005 *Riv. Nuovo Cimento* **28** 1
[20] Milants K, Hendrickx P and Pattyn H 1993 *Nucl. Instrum. Methods Phys. Res.* B **80/81** 1014
[21] Lay G Le, Hricovini K and Bonnet J E 1989 *Appl. Surf. Sci.* **41/42** 25
[22] Ziegler J F, Biersack J P and Littmark U 1985 *The Stopping and Ranges of Ions in Solids* (New York: Pergamon) www.srim.com
[23] Bras W, Dolbnya I P, Detollenaere D, Van Tol R, Malfois M, Greaves G N, Ryan A J and Heeley E 2003 *J. Appl. Cryst.* **36** 791
[24] Huang T C, Toraya H, Blanton T N and Wu Y 1993 *J. Appl. Cryst.* **26** 180
[25] Ke X X, Bals S, Negreira A R, Hantschel T, Bender H and Van Tendeloo G 2009 *Ultramicroscopy* **109** 1353
[26] Gilbert P 1972 *J. Theor. Biol.* **36** 105
[27] Yamaguchi S, Kariya M, Nitta S, Takeuchi T, Wetzel C, Amano H and Akasaki I 1999 *J. Appl. Phys.* **85** 7682
[28] Hays J, Punnoose A, Baldner R, Engelhard M H, Peloquin J and Reddy K M 2005 *Phys. Rev.* B **72** 075203
[29] Deguledre C, Kuri G, Borca C N and Grolimund D 2009 *Corros. Sci.* **51** 1690
[30] Boswell F W C 1951 *Proc. Phys. Soc.* A **64** 465
[31] Wu M F, Vantomme A, Pattyn H, Langouche G, Yang Q and Wang Q 1996 *J. Appl. Phys.* **80** 5713
[32] Glatter O and Kratky O 1982 *Small Angle X-ray Scattering* (London: Academic)
[33] Lpez-Honorato E, Zhang H, Yang D and Xiao P 2011 *J. Am. Ceram. Soc.* **94** 3064
[34] Amerkura H, Ohnuma M, Kishimoto N, Buchal Ch and Mantl S 2008 *J Appl. Phys.* **104** 114309
[35] Marchi G De, Mattei G, Mazzoldi P, Sada C and Miotello A 2002 *J. Appl. Phys.* **92** 4249
[36] Nozawa K, Delville M-H, Ushiki H, Panizza P and Delville J-P 2005 *Phys. Rev.* E **72** 011404
[37] Leubner I H, Jagannathan R and Wey J S 1980 *Photograph. Sci. Eng.* **24** 268
[38] Leubner I H 1987 *J. Phys. Chem.* **91** 6069
[39] Lifshitz I M and Slyozov V V 1961 *J. Phys. Chem. Solids* **19** 35
[40] Wagner V C 1961 *Z. Elektrochem.* **65** 581
[41] Johnson E, Johansen A, Sarholt L and Dahmen U 1999 *Nucl. Instrum. Methods Phys. Res.* B **148** 1034
[42] Luce F P, Kremer F, Reboh S, Fabrim Z E, Sanchez D F, Zawislak F C and Fichtner P F P 2011 *J. Appl. Phys.* **109** 014320
[43] Kittel C 2005 *Introduction to Solid State Physics* (New York: Wiley)